

Constraining the parameters of the pulsar wind nebula DA 495 and its pulsar with *Chandra* and *XMM-Newton*

A. Karpova^{1,2*}, D. Zyuzin¹, A. Danilenko¹, Yu. Shibano^{1,2}

¹Ioffe Institute, Politekhnikeskaya 26, St. Petersburg, 194021, Russia

²Peter the Great St.Petersburg Polytechnic University, Politekhnikeskaya 29, St. Petersburg, 195251, Russia

Accepted XXX. Received YYY; in original form ZZZ

ABSTRACT

We present spectral and timing analyses of the X-ray emission from the pulsar wind nebula DA 495 and its central object, J1952.2+2925, suggested to be the pulsar, using archival *Chandra* and *XMM-Newton* data. J1952.2+2925 has a pure thermal spectrum which is equally well fitted either by the blackbody model with a temperature of ≈ 215 eV and an emitting area radius of ≈ 0.6 km or by magnetized neutron star atmosphere models with temperatures of 80–90 eV. In the latter case the thermal emission can come from the entire neutron star surface which temperature is consistent with standard neutron star cooling scenarios. We place also an upper limit on the J1952.2+2925 nonthermal flux. The derived spectral parameters are generally compatible with published ones based only on the *Chandra* data, but they are much more accurate due to the inclusion of *XMM-Newton* data. No pulsations were found and we placed an upper limit for the J1952.2+2925 pulsed emission fraction of 40 per cent. Utilizing the interstellar absorption–distance relation, we estimated the distance to DA 495, which can be as large as 5 kpc if J1952.2+2925 emission is described by the atmosphere models. We compiled possible multi-wavelength spectra of the nebula including radio data; they depend on the spectral model of the central object. Comparing the results with other pulsar plus wind nebula systems we set reasonable constraints on the J1952.2+2925 spin-down luminosity and age. We suggest that the *Fermi* source 3FGL J1951.6+2926 is the likely γ -ray counterpart of J1952.2+2925.

Key words: ISM: supernova remnants – ISM: individual: G65.7+1.2 – stars: neutron – stars: individual: J1952.2+2925

1 INTRODUCTION

More than 50 pulsar wind nebulae (PWNe) are currently known (e.g., Kargaltsev & Pavlov 2008). The Crab nebula is a classical example of young PWNe which is the best studied from the radio to the TeV range. However, other PWNe, not yet studied in such details, show a variety of individual properties different from the Crab, which are determined by their pulsar parameters, evolution stages and surroundings, including the interstellar medium and the supernova ejecta. Studying such PWNe is crucial for understanding the properties of their central ‘engines’, the interaction of the relativistic pulsar wind with surroundings and particle acceleration mechanisms (Gaensler & Slane 2006). Multiwavelength observations of the PWNe at late evolutionary stages and different environment are still rare but they are particularly important for comparison with the Crab and various theoretical models of evolution of these objects (Gelfand et al.

2009; Tanaka & Takahara 2010; Chevalier & Reynolds 2011, and references therein).

DA 495 (G65.7+1.2) appears to be an example of an evolved PWN. It was discovered in the radio (Galt & Kennedy 1968). Detailed radio observations showed that DA 495 has an uncommon annular morphology with a central flux deficit within ~ 2 arcmin from the centre, dubbed the radio ‘hole’ (Landecker & Caswell 1983). The full extent of DA 495 is about 25 arcmin and the radio emissivity decreases gradually to its outer edge without any evidence of the supernova remnant (SNR) shell existence (see Fig. 1, bottom panel). A possible association with the open cluster NGC 6834 implied a distance D to the object of ≈ 2.1 kpc (Landecker & Caswell 1983). H I absorption measurements and a flat rotation model for the Milky Way provided D within a range of 1–1.5 kpc, depending on the adopted Galactocentric radius for the Sun (Kothes et al. 2004, 2008). Kothes et al. (2008) found a spectral break at 1.3 GHz, the lowest for the known PWNe, with spectral indices $\alpha_\nu = 0.45 \pm 0.20$ and $\alpha_\nu = 0.87 \pm 0.10$ below and above

* E-mail: annakarpova1989@gmail.com

the break, respectively¹. They also suggested that DA 495 is about 20 kyr old. No detection of an associated pulsar in the radio and γ -rays was reported.

In X-rays, *ROSAT* and *ASCA* observations of DA 495 revealed a faint compact source, 1WGA J1952.2+2925 (hereafter J1952), which is apparently surrounded by a diffuse non-thermal emission and is projected on the edge of the radio hole (Arzoumanian et al. 2004) (see Fig. 1). It was proposed to be a magnetospherically active neutron star (NS) powering the PWN, although only an upper limit on the pulsed emission fraction of 50 per cent for periods $\gtrsim 30$ ms was derived from the analysis of the *ASCA* data. The compact source J1952 and its diffuse emission were later firmly confirmed by *Chandra* high spatial resolution observations (Arzoumanian et al. 2008). It was established that J1952 is the point source located in the centre of the X-ray nebula with an extent of $\sim 40''$. The nebula does not show any Crab-like torus+jet structure, however its spectrum is described by a power law with a photon index $\Gamma = 1.6 \pm 0.3$ typical for PWNe. The latter allowed to state that it is the X-ray counterpart of the DA 495 PWN. J1952, presumably the pulsar, has a pure thermal spectrum. It can be described either by the blackbody model with a temperature $T \approx 2.5$ MK and an emitting area radius $R \approx 0.3$ km or by the neutron star atmosphere (NSA) model (Zavlin, Pavlov & Shibano 1996) for a NS with the effective temperature of ≈ 1 MK and the radius of 10 km. The interstellar absorption column density for the former and latter cases was $\approx 2.3 \times 10^{21}$ and $6.0 \times 10^{21} \text{ cm}^{-2}$, respectively, which is a factor of 1.3–3.5 lower than the entire Galactic absorption in this direction. Because of small count statistics, the spectral parameters were poorly constrained. In addition, two key parameters, the distance and the pulsar spin-down energy loss \dot{E} , also remained uncertain, which did not allow to establish firmly the DA 495 PWN evolution stage. Finally, a high energy source 3FGL J1951.6+2926 recently detected with *Fermi*/LAT was proposed as a possible γ -ray counterpart (Acero et al. 2015) of the nebula.

Here we report a simultaneous analysis of the *Chandra*² and unpublished *XMM-Newton*³ X-ray archival data on DA 495. We also include in our analysis the extinction–distance relation towards J1952. This allows us to improve considerably the count statistics, to get an independent DA 495 distance estimate and to set more stringent constraints on the PWN and pulsar parameters. We also use high temporal resolution *XMM-Newton*/EPIC-pn data to search for periodic pulsations from J1952 and derive a more stringent upper limit on its pulsed emission fraction. The details of observations are described in Sect. 2. The timing analysis is presented in Sect. 3. The extinction–distance relation and spectral analysis are described in Sect. 4 and 5. In Sect. 6 we discuss our results, compare them with the DA 495 radio and γ data and the data for other pulsar+PWN systems. A summary is given in Sect. 7.

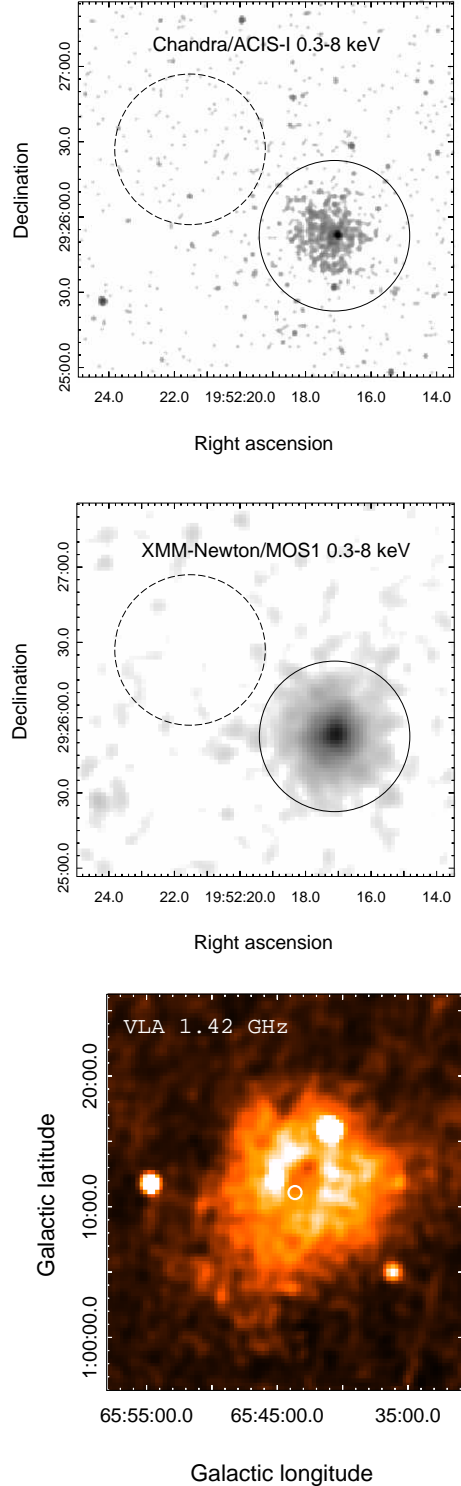


Figure 1. $2'.5 \times 2'.5$ X-ray *Chandra* (top), *XMM-Newton* (middle) and $30' \times 27'$ radio VLA (bottom) images of DA 495 in 0.3–8 keV range and at 1.42 GHz, respectively. The *Chandra* image was smoothed with a 3 pixel Gaussian kernel (logarithmic brightness scale is used). J1952 is clearly seen in the centre of the PWN in X-rays. The *XMM-Newton* image was binned to a pixel size of $1''.6$ and smoothed with a 3 pixel Gaussian kernel (square root brightness scale is used). Solid and dashed circles depict the extraction region for the PWN+J1952 and background, respectively. The white circle in the radio image shows the position and extent of DA 495 in X-rays.

¹ Assuming the spectral flux $F_\nu \propto \nu^{-\alpha_\nu}$, where ν is the frequency.

² PI Arzoumanian, *Chandra*/ACIS-I, ObsID 3900

³ PI Arzoumanian, *XMM-Newton*/EPIC, ObsID 0406960101

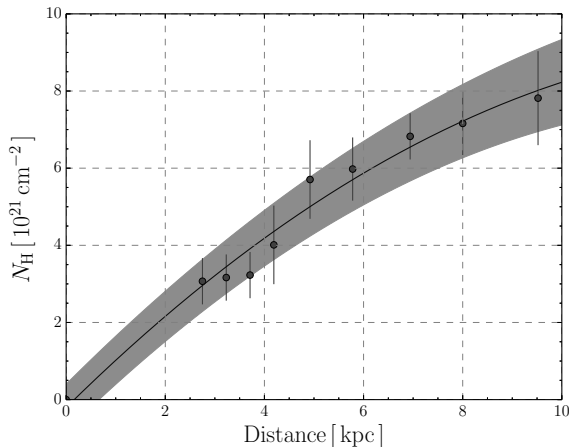


Figure 2. Data points show empirical N_{H} –distance relation for the DA 495 direction derived using Marshall et al. (2006) extinction map. The error bars represent 1σ uncertainties. The solid line and gray filled region are smoothing spline approximations to the data points and their uncertainties, respectively.

2 THE X-RAY DATA

The *XMM-Newton* observations of DA 495 were carried on 2007 April 21 with total exposure of about 50 ks. The EPIC-MOS cameras were operated in the Full Frame Mode with the medium filter setting, and the EPIC-pn camera was operated in the Small Window Mode with the thin filter. The XMM-SAS v.13.5.0 software was used to process the data. We selected single and double pixel events ($\text{PATTERN} \leq 4$) for the EPIC-pn and single to quadruple-pixel events ($\text{PATTERN} \leq 12$) for the EPIC-MOS data. We removed periods of background flares using 10–12 keV and 12–14 keV light curves for the MOS and pn data, respectively.

We also used the observation of DA 495 made with *Chandra*/ACIS-I on 2002 December 9. The data mode was VFaint, the exposure mode was TE and the total exposure was 24.8 ks. The CIAO v.4.6 CHANDRA_REPRO tool with CALDB v.4.6.1 was used to reprocess the data. We found no background flares in this observation. The resulting effective exposures are presented in Table 1.

3 TIMING ANALYSIS

The EPIC-pn data, which have the time resolution of 5.6 ms, were used to search for pulsations from J1952. Event times were corrected to the solar system barycentre using the SAS task BARYCEN and J1952 *Chandra* coordinates obtained with the CIAO tool WAVDETECT (RA = 298° 0710, Dec = 29° 4313). We used a circular region of 20 arcsec around J1952 to extract its light curve. The SAS task EPICLCCORR was used for background subtraction and correction for vignetting, bad pixels and quantum efficiency. The resulting light curve contained about 1060 source counts in the 0.5–1.4 keV energy band. We chose this energy range to minimize the contribution of the PWN emission and since J1952 dominates at these energies (see Sect. 5). After that we performed a Fast Fourier Transform (FFT) analysis using stan-

dard XRONOS v.5.22⁴ task POWSPEC. No pulsations were found. We derived an upper limit for the pulsed fraction (PF) of 40 per cent (at the 99 per cent confidence level) for periods $\gtrsim 12$ ms following the procedure described by Vaughan et al. (1994).

4 DISTANCE AND INTERSTELLAR EXTINCTION

It is possible to estimate the distance to DA 495 using the absorption column density N_{H} –distance relation along its line of sight. To do this we use the interstellar extinction distribution obtained by Marshall et al. (2006) for the direction towards DA 495. They used the 2MASS survey along with the Besançon model of population synthesis (Robin et al. 2003) to calculate the K_s extinction dependence on distance along different lines of sight. We obtained this dependence from the Vizier Service⁵ for the DA 495 direction and then transformed the extinctions to the column densities N_{H} utilizing a relation $A_{K_s}/A_V \approx 0.1$ (see e.g. Rieke & Lebofsky 1985) and a standard empirical N_{H} – A_V relation (Predehl & Schmitt 1995). The resulting N_{H} –distance dependence is shown in Fig. 2. The N_{H} –distance relation and its uncertainties were approximated by smoothing splines.

5 ANALYSIS OF THE X-RAY SPECTRA

The *Chandra* and *XMM-Newton* images of DA 495 for the 0.3–8 keV energy range are shown in the top and middle panels of Fig. 1, respectively. In the *Chandra* image the extended PWN is seen around the point source J1952. Due to a moderate angular resolution of *XMM-Newton* the PWN+J1952 system appears to be slightly more extended⁶ and the point source is blended with the PWN. Therefore, to perform spectral analysis of J1952 and the PWN we used their individual spectra extracted from the *Chandra* data, while from the *XMM-Newton* data we extracted the spectrum corresponding to the combined PWN+J1952 emission. For the latter we chose 30 arcsec aperture encircling the whole PWN emission (see Fig. 1) using EVSELECT tool. We then used SAS tasks RMFGEN and ARFGEN to generate the redistribution matrix and ancillary response files for the MOS1, MOS2 and pn detectors. For the *Chandra* data set we extracted the J1952 spectrum from a circular region of 1.5-pixel radius centred at this source and the PWN spectrum from the same circular region as for *XMM-Newton* excluding 1 arcsec radius region around J1952 using SPEXTRACT tool. Background was taken from the region free from any sources (see Fig. 1). All spectra were grouped to ensure ≥ 5 counts per energy bin. The resulting number of counts in the apertures and background-subtracted source count rates are presented in Table 1.

⁴ <http://heasarc.gsfc.nasa.gov/docs/xanadu/xronos/xronos.html>

⁵ <http://vizier.u-strasbg.fr/viz-bin/VizieR-3?-source=J/A%2bA/453/635/>

⁶ We have searched for a fainter PWN emission at larger spacial scales in the *XMM-Newton* images but not found it.

Table 1. Resulting *Chandra* and *XMM-Newton* exposure times, number of counts and background-subtracted count rates in 0.3–10 keV energy band for different instruments and source apertures for the J1952, PWN and J1952+PWN after data reprocessing, filtering and correction for background flares.

| Instrument Detector | <i>Chandra</i> ACIS-I | | <i>XMM-Newton</i> EPIC/ MOS1 MOS2 pn | | | |
|--|--------------------------|---------|--|-----------|----------|----------|
| | Source | J1952 | PWN | J1952+PWN | | |
| exposure (ks) | | 24.8 | 24.8 | 46.5 | 47.5 | 33.7 |
| counts within the aperture (see text) | | 145 | 577 | 1300 | 1282 | 4194 |
| background-subtracted count rate (cts ks ⁻¹) | | 5.8±0.5 | 19.6±1.0 | 22.9±0.8 | 22.2±0.8 | 74.4±2.2 |

Table 2. Best-fit spectral parameters. All errors correspond to 90 per cent credible intervals. R and T are given as seen by a distant observer. The PWN luminosity L_{PWN} is in the 0.5–8 keV range. K_{PWN} is the normalisation constant for the PL model of the PWN. F_{J1952} is the point source bolometric flux. $L_{\text{J1952}}^{\text{pl}}$ is a 3σ upper limit on the non-thermal component of the point source luminosity in 0.5–8 keV band.

| Model | N_{H} , 10^{21} cm ⁻² | D , kpc | R , km | T , eV | Γ_{PWN} | K_{PWN} , 10^{-5} ph keV ⁻¹ cm ⁻² | $\text{Log}F_{\text{J1952}}$, erg s ⁻¹ cm ⁻² | $\text{Log}L_{\text{J1952}}^{\text{pl}}$, erg s ⁻¹ | $\text{Log}L_{\text{PWN}}$, erg s ⁻¹ | χ^2/dof |
|-----------------------------|--|---------------------|---------------------|-------------------|------------------------|--|--|---|---|---------------------|
| 1. BB | $2.6^{+0.5}_{-0.4}$ | $2.4^{+1.3}_{-1.1}$ | $0.6^{+0.6}_{-0.3}$ | 215^{+23}_{-23} | $1.71^{+0.12}_{-0.12}$ | $4.4^{+0.7}_{-0.6}$ | $-12.94^{+0.14}_{-0.11}$ | < 31.51 | $32.22^{+0.38}_{-0.49}$ | 455/461 |
| 2. NSMAX $B = 10^{12}$ G | $3.5^{+0.7}_{-0.6}$ | $3.3^{+1.7}_{-1.3}$ | 10^{+21}_{-7} | 76^{+19}_{-16} | $1.83^{+0.14}_{-0.13}$ | $5.1^{+0.9}_{-0.7}$ | $-12.47^{+0.35}_{-0.26}$ | < 31.66 | $32.53^{+0.37}_{-0.45}$ | 455/461 |
| 3. NSMAX $B = 10^{13}$ G | $3.4^{+0.7}_{-0.6}$ | $3.2^{+1.5}_{-1.2}$ | $6^{+9}_{-3.5}$ | 91^{+17}_{-15} | $1.82^{+0.13}_{-0.13}$ | $5.1^{+0.8}_{-0.6}$ | $-12.57^{+0.27}_{-0.20}$ | < 31.72 | $32.50^{+0.35}_{-0.42}$ | 454/461 |

A power law (PL) was used to model the PWN emission. For the J1952 spectrum, we tried the neutron star atmosphere models NSA (Zavlin et al. 1996) and NSMAX (Ho, Potekhin & Chabrier 2008) with a gravitational redshift $z_g + 1 = 1.21$ and magnetic fields $B = 10^{12}$ G and $B = 10^{13}$ G and the blackbody (BB) model. For the interstellar absorption, we used the XSPEC photoelectric absorption PHABS model with default cross-sections BCMC (Balucinska-Church & McCammon 1992) and abundances ANGR (Anders & Grevesse 1989). We fitted XMM-Newton and Chandra spectra of the J1952+PWN, J1952 and PWN simultaneously in 0.3–10 keV energy range.

We fit the data using the Bayesian inference with the N_H –distance relation as a prior. We obtained samples from the posterior distribution by the Markov chain Monte-Carlo (MCMC) sampler developed by Goodman & Weare (2010) and implemented as a python package EMCEE by Foreman-Mackey et al. (2013). We obtained 100000 samples which is enough compared with autocorrelation time (50–80). The procedure is similar to that utilised by Kirichenko et al. (2015). Posterior median values of the spectral parameters with 90 per cent credible intervals are presented in Table 2, where the models differ only by the thermal components applied and are named according to that. Since the best-fit parameters do not depend strongly on the specific type of atmospheric models, i.e., NSA or NSMAX, we present the results only for the BB and NSMAX models. The χ^2 values per degree of freedom (dof) show that all models describe the data equally well. For both models our results are generally consistent with results of Arzoumanian et al. (2008), however they are several times less uncertain (cf. their Table 1) due to the better count statistics. The example of the fit for the model 2 from Table 2 is shown in Fig. 3.

It is important, that using the Bayesian approach and N_H – D relation, we were able to derive the values of D and the J1952 emitting area radius R independently, as opposed to their ratios obtained traditionally from such fits. For the NSMAX models, $R = 10^{+21}_{-7}$ km ($B = 10^{12}$ G) and $R = 6^{+9}_{-3.5}$ km ($B = 10^{13}$ G) imply that the thermal emission originates from the entire NS surface. For the BB model, the emitting area is significantly smaller, $R = 0.6^{+0.6}_{-0.3}$ km, and the radiation likely comes from a hot polar cap of the pulsar. To derive an upper limit on the temperature of the entire NS surface in the latter case, we added a second BB component to the best-fit model. The radius of the emitting area was fixed at a conventional NS radius of 13 km. We obtained a 3σ upper limit on the entire surface temperature of ≈ 60 eV.

For the J1952 spectrum we also tried the PL model that provided a worse fit quality ($\chi^2/\text{dof}=489/461$) and resulted in a too large photon index $\Gamma = 4.4^{+0.6}_{-0.5}$, not typical for pulsars (see e.g. Li, Lu & Li 2008).

Besides, we added a power law component to the thermal component for J1952 to estimate an upper limit on the pulsar non-thermal luminosity $L_{\text{J1952}}^{\text{pl}}$. In current data this emission component is not resolved within the non-thermal PWN background. The photon index Γ was assumed to lie in the range $0.5 \leq \Gamma \leq 2.0$ typical for other pulsars. The resulting values of $L_{\text{J1952}}^{\text{pl}}$ are also presented in Table 2.

6 DISCUSSION

We used high temporal resolution XMM-Newton/EPIC-pn archival data to search for pulsations from the NS J1952. No pulsations were detected. However, we set a more stringent upper limit for the pulsed fraction of 40 per cent (99 per cent confidence) in a wider period range of $\gtrsim 12$ ms (Sect. 3) than previous estimates based on the ASCA data (Arzoumanian et al. 2004). We confirmed the result of Arzoumanian et al. (2008) that only the thermal emission component is detected in the X-ray spectrum of J1952 and better constrained its parameters. For the BB model the emitting area radius is ≈ 0.6 km (see Table 2) showing that the thermal component originates from a small hot spot on the NS surface with $T \approx 215$ eV, which is typical for pulsar hot polar caps. On the other hand, the NSMAX models suggest that the emission comes from the entire NS surface. We cannot assert definitely which case is true for J1952. The detection of the pulsations, the phase-resolved spectral analysis and the analysis of pulse profile shapes could help to solve this problem. Our upper limit on the PF of 40 per cent is higher than typical PFs of 10–30 per cent detected for the thermal emission from entire surfaces of other NSs (Zavlin 2007; Pavlov & Zavlin 2000).

The interstellar absorption–distance relation (Sect. 4) allowed us to estimate the distance to DA 495. For the BB model $D = 2.4^{+1.3}_{-1.1}$ kpc. The NS atmosphere models suggest a larger distance: $3.3^{+1.7}_{-1.3}$ kpc, if the J1952 magnetic field is 10^{12} G, or $3.2^{+1.5}_{-1.2}$ kpc, if it is 10^{13} G (Table 2). Within uncertainties, all these values are consistent with one of the previous estimates, $D \approx 2.1$ kpc, assuming possible association of DA 495 with the open cluster NGC 6834 (Landecker & Caswell 1983). Another distance estimate of 1.0 ± 0.4 kpc is compatible only with the BB model. It was based on the H I absorption feature in the DA 495 polarized radio continuum emission with a systemic velocity of $+12$ km s $^{-1}$, which is likely associated with the Galactic Local Arm (Kothes et al. 2008). The authors also mentioned a distance of 5 kpc as an alternative interpretation of the feature. This is compatible at the upper confidence level with the result provided by our atmospheric fits. However, they argued that this distance is inconsistent with the low foreground absorbing column density obtained by Arzoumanian et al. (2008) from Chandra X-ray data using the BB model and with the absence of the H I absorption from the Local Arm tangent point expected to be at the velocity of about $+20$ km s $^{-1}$. We note, that the latter absorption cannot be completely excluded due to a low signal-to-noise ratio of the radio data. The atmospheric models cannot be also ignored in the above argument. Moreover, recent trigonometric parallax measurements of high mass star forming regions show that the Local Arm extends beyond 5 kpc with a shallow pitch angle of $\approx 10^\circ$ between $l \approx 72^\circ$ and 52° toward the Perseus Arm (Reid et al. 2014; Xu et al. 2013). It is possibly a separate branch of the Perseus, connecting with it at a distance of about 6.5 kpc (see fig. 12 from Xu et al. 2013). DA 495 with $l \approx 65.7$ is obviously located within the new Local Arm longitude range. Therefore, the gas within this arm can be a natural source of the larger foreground X-ray absorption at the larger DA 495 distance suggested by the atmospheric models (Table 2).

The PWN spectral indices α_ν derived from our X-ray

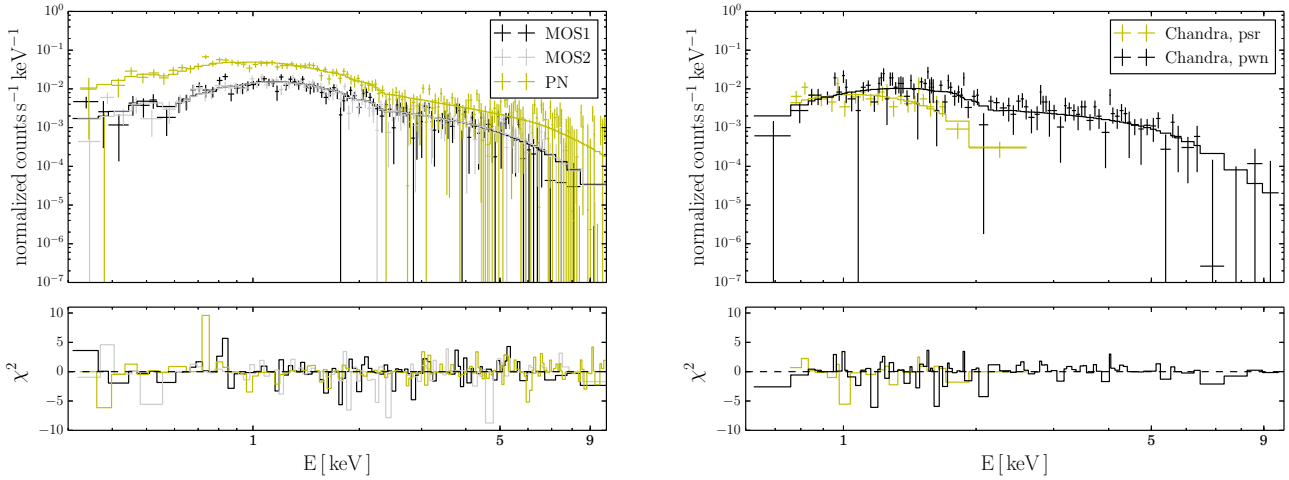


Figure 3. Observed X-ray spectrum of the DA 495 pulsar+PWN system obtained with *XMM-Newton* (top-left) and *Chandra* (top-right). The data for different instruments/sources are shown by different crosses, as indicated in the inserts. Lines show the best-fit model. Bottom: Fit residuals.

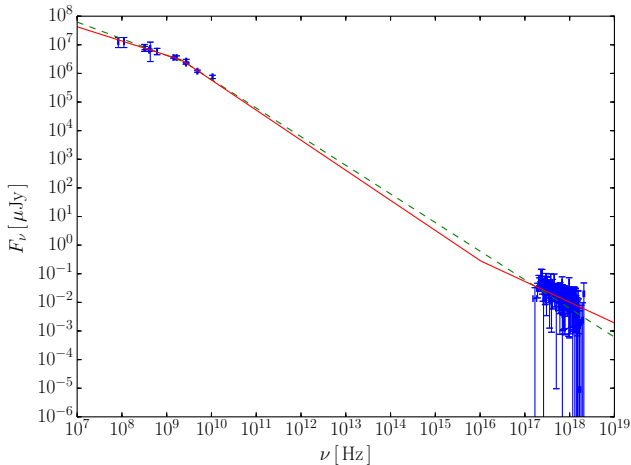


Figure 4. Unabsorbed spectrum of the DA 495 PWN from the radio to X-rays. The X-ray spectrum of the associated pulsar J1957 is fitted by the BB model. The dashed and solid lines are the best fits to the PWN data by the broken PL model with the single and the double-knee breaks, respectively. The position of the second high frequency spectral break is poorly defined (see text for details), it is fixed here for illustrative purposes.

fits are 0.71 ± 0.12 , 0.83 ± 0.13 and 0.82 ± 0.13 (90 per cent confidence) when the thermal component from the NS was described by the BB and atmosphere models with $B = 10^{12}$ G and 10^{13} G, respectively. These values are in agreement within uncertainties with each other and with $\alpha_\nu = 0.87 \pm 0.10$ (68 per cent confidence) obtained from the radio data for frequencies above the 1.3 GHz break (Kotthes et al. 2008). However, a marginal spectral flattening in X-rays, particularly in the BB case, cannot be excluded, suggesting a second break. To examine whether an additional break between the radio and X-rays is needed or not, we tried to fit the X-ray spectra together with the radio data taken from Kotthes et al. (2008). At first, the PWN spectrum was fitted by a broken power law (BPL) with a single break. In all

cases the break in the radio was $2.1^{+0.8}_{-0.5}$ GHz. This value is higher than that of Kotthes et al. (2008) due to the addition of the X-ray data; using only the radio data we reproduced their result of ≈ 1.3 GHz. The spectral indices $\alpha_{\nu 1}$ and $\alpha_{\nu 2}$ before and above this break were 0.61 ± 0.07 and 1.00 ± 0.01 for the NSMAX+BPL models and 0.58 ± 0.07 and 1.00 ± 0.01 for the BB+BPL model. Then we included a second break to the PWN model. For the NSMAX+BPL models, the resulting spectral indices $\alpha_{\nu 1}$ and $\alpha_{\nu 2}$ before and above the break at 2 GHz and the spectral index $\alpha_{\nu 3}$ above the second break were $0.50^{+0.09}_{-0.12}$, $1.02^{+0.07}_{-0.04}$ and $0.84^{+0.11}_{-0.12}$ in the case of $B = 10^{12}$ G and $0.50^{+0.10}_{-0.13}$, $1.02^{+0.10}_{-0.04}$ and $0.83^{+0.15}_{-0.13}$ in the case of $B = 10^{13}$ G. For the BB+BPL model, $\alpha_{\nu 1} = 0.5^{+0.09}_{-0.11}$, $\alpha_{\nu 2} = 1.05^{+0.11}_{-0.05}$ and $\alpha_{\nu 3} = 0.72^{+0.11}_{-0.11}$. We carried out an F-test using the XSPEC FTEST routine to compare models with single and double-knee breaks. The resulted probabilities for the NSMAX+BPL were ≈ 0.1 for both values of magnetic field demonstrating that the second break is not needed. On the other hand, the probability for the BB+BPL model is 0.03 providing a marginal evidence that the PWN spectrum in X-rays indeed becomes flatter although the second break position is poorly defined and lies in a range of $10^{14} - 10^{17}$ Hz, somewhere between the mid-infrared and X-rays. The best fits to the data by the BB+BPL model with single and double-knee breaks are presented in Fig. 4.

Assuming that the spectral break at ≈ 2 GHz in DA 495 emission arises from the synchrotron cooling and using the formula from Ginzburg & Syrovatskii (1965),

$$\nu_c(\text{GHz}) \approx 1.2 \times 10^3 B_{\text{mG}}^{-3} t_{\text{kyr}}^{-2}, \quad (1)$$

where ν_c is the cooling frequency, B_{mG} is the PWN magnetic field in milligauss, and t_{kyr} is the PWN age in kyr, we can estimate the age of DA 495. The synchrotron lifetime is $\tau_{\text{synch}} \approx 3.3 R_{\text{pc}} c / v$ yr, where R_{pc} is the emitting area radius in pc, v is the velocity of the pulsar wind particles and c is the speed of light. At a distance of about 1.5 kpc, which is close to the low boundary obtained from the X-ray spectral fits, $R_{\text{pc}} = 0.15 D_{1.5\text{kpc}}$, which corresponds to the 20 arcsec angular radius of the X-ray PWN, and

$\tau_{\text{synch}} \approx 1.7D_{1.5\text{kpc}} \text{ yr}$, assuming a typical velocity $v = 0.3c$ (Kennel & Coroniti 1984). On the other hand, at an X-ray photon energy $E = 1.5 \text{ keV}$, $\tau_{\text{synch}} = 1.2 E_{\text{keV}}^{-1/2} B_{\text{mG}}^{-3/2} \approx B_{\text{mG}}^{-3/2}$. This yields $B_{\text{mG}} \approx 0.7D_{1.5\text{kpc}}^{-2/3}$ and the expression (1) implies the DA 495 age $t_{\text{kyr}} \approx 40D_{1.5\text{kpc}}$. At the maximum distance of about 5 kpc we obtain $B_{\text{mG}} \approx 0.3$, which is comparable to that of the Crab Nebula, and a maximum age $t_{\text{kyr}} \approx 130$. These simplified estimates imply that DA 495 may be a factor of 2–6 older than it was suggested by Kothes et al. (2008).

The distance estimate allowed us to derive the PWN luminosity L_{pwn} and the 3σ upper limit on the non-thermal luminosity of its pulsar $L_{\text{J1952}}^{\text{pl}}$ (Table 2). These parameters can be used to estimate the J1952 spin-down luminosity \dot{E} utilizing the empirical dependencies $L_{\text{pwn}}(\dot{E})$, $L_{\text{psr}}^{\text{pl}}(\dot{E})$ and $L_{\text{pwn}}(L_{\text{psr}}^{\text{pl}})$ obtained for 0.5–8 keV band by Kargaltsev & Pavlov (2008) using the data for other pulsars+PWN systems (Fig. 5). For completeness, we added to these data PSR J2022+3842 with its PWN G76.9+1.0 (Arzoumanian et al. 2011; Arumugasamy et al. 2014) marked in Fig. 5 by a triangle. Summarising the results for all three models presented in Table 2, $\log L_{\text{pwn}}$ for DA 485 lies in the range of 31.7–32.9 (horizontal solid lines in the top and bottom panels of Fig. 5), which implies $\log \dot{E} = 32.7\text{--}37.9$ for the X-ray efficiency range $\eta_{\text{X}}^{\text{pwn}} = 10^{-5} - 10^{-1}$ based on the data for all PWNe observed (the grey shaded region between the horizontal solid lines in the top panel). Using the respective empirical luminosity vs age dependence $L_{\text{pwn}}(t)$ for the same PWNe set (Fig. 6, left panel)⁷ and the DA 495 L_{pwn} allowed range, we can obtain the possible age range of DA 495 as $7 \lesssim t_{\text{kyr}} \lesssim 155$ (the grey region between two vertical dashed lines in the left panel of Fig. 6)⁸. This age range is slightly wider than that based on the simple synchrotron cooling scenario. At the same time, the derived upper limit on the pulsar nonthermal luminosity $\log L_{\text{J1952}}^{\text{pl}} < 31.7$ (the horizontal solid line in the middle panel of Fig. 5) suggests $\log \dot{E} < 37.1$ for the pulsar efficiency range $\eta_{\text{X}}^{\text{psr}} \gtrsim 10^{-5.4}$ based on the data for all pulsars (the grey region in the middle panel of Fig. 5). The lower limit for $\eta_{\text{X}}^{\text{psr}}$ (the dotted line in the middle panel of Fig. 5) corresponds to the Vela pulsar X-ray efficiency, which is known to be very under-luminous in X-rays. Consequently, a real $\log \dot{E}$ value likely lies in the range of 32.7–37.1 where the allowed ranges of \dot{E} for the PWN and J1952 overlap. This range boundaries are shown by solid lines in the $\dot{E}(t)$ empirical dependence in the right panel of Fig. 6. On the other hand, the $L_{\text{pwn}}(L_{\text{psr}}^{\text{pl}})$ dependence allows us to set a lower limit of ≈ 30.7 on the J1952 non-thermal luminosity (the vertical dashed line in the bottom panel of Fig. 5). This value is also shown by the horizontal dashed line in the middle panel of Fig. 5. Finally, the $\dot{E}(t)$ empirical dependence in the right panel of Fig. 6 and the estimated age range (the vertical dashed lines in

⁷ For age t , the pulsar spin-down ages are used except for the cases when the true ages are known from respective SNR studies: Crab, J1833–1034 (Bietenholz & Bartel 2008), J1811–1925 (Roberts et al. 2003), B1951+32 (Migliazzo et al. 2002), J0538+2817 (Ng et al. 2007).

⁸ At this point we excluded PSR J1119–6127, marked by the star symbol in the left panel of Fig. 6, as a peculiar high-B pulsar with a very faint PWN (Gonzalez & Safi-Harb 2003).

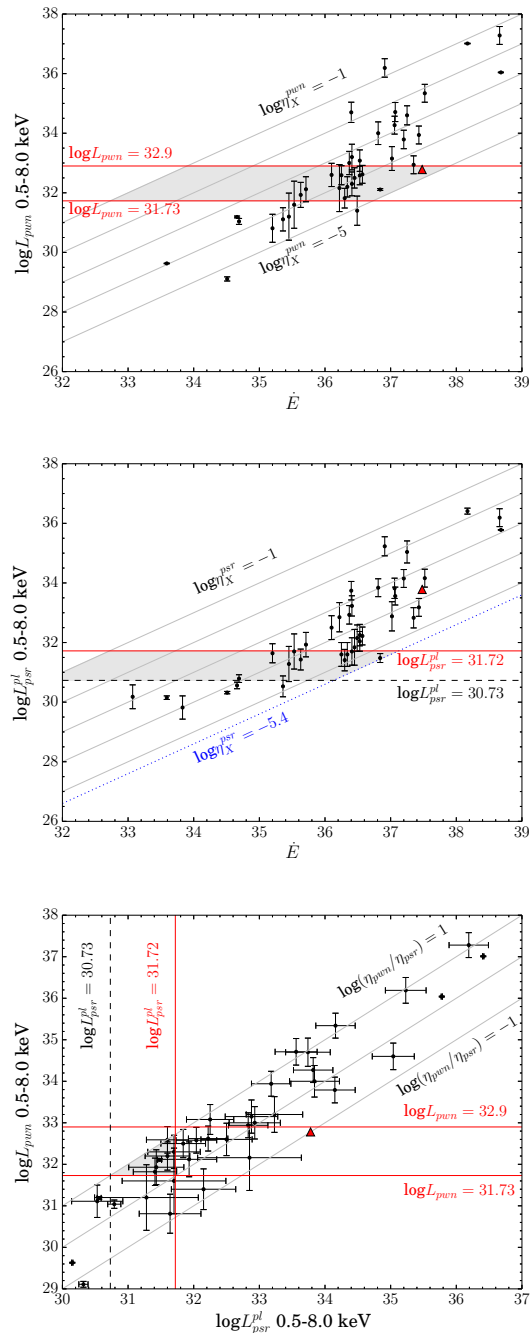


Figure 5. *Top panel:* X-ray luminosities of PWNe vs the spin-down luminosity \dot{E} . *Middle panel:* the same as is in the top panel but for X-ray non-thermal luminosities of the pulsars powering the PWNe. *Bottom panel:* X-ray luminosities of the same PWNe vs pulsar X-ray non-thermal luminosity. Error-bars include 40 per cent systematic distance uncertainties for objects where parallax was not measured. Grey solid lines show constant efficiency levels η for the PWNe and PSRs and their ratio as indicated in the plots. Horizontal solid lines correspond to the DA 495 PWN luminosity lower and upper bounds and the upper limit on the J1952 pulsar non-thermal luminosity obtained from the X-ray spectral fits. Their values are presented in the plots. The dotted line in the middle panel indicates the lowest efficiency level corresponding to the Vela pulsar. The black dashed lines represents the lower bound of the J1952 pulsar non-thermal luminosity. The regions where the DA 495 PWN and its pulsar are expected to locate are filled by the grey colour.

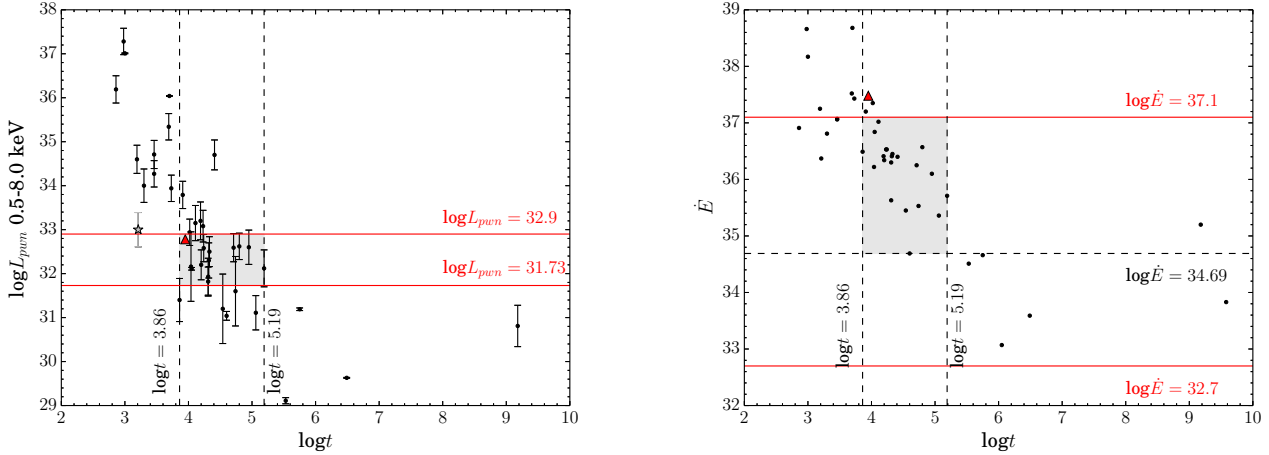


Figure 6. L_{pwn} for the same PWNe as in Fig. 5 (left) and respective \dot{E} (right) vs age t . Solid lines show the DA 495 PWN luminosity bounds derived from the fits and its spin-down luminosity range estimated from $L_{\text{pwn}}(\dot{E})$ and $L_{\text{psr}}^{\text{pl}}(\dot{E})$ dependencies presented in Fig. 5. The vertical dashed lines show a possible age bounds for DA 495 and the horizontal dashed line in the *right panel* demonstrates its possible spin-down luminosity lower bound based on the age bounds and $\dot{E}(t)$ distribution for other pulsars. The regions where the DA 495 PWN and its pulsar are expected to locate are filled by the grey colour.

this plot) suggest a more narrow $\log \dot{E}$ range of 34.7–37.1 corresponding to the grey region in this panel between the upper solid and horizontal dashed lines. This appears to be the most reasonable DA 495 \dot{E} range summarising all data available for DA 495 and other PWN+pulsar systems.

Comparing thermal properties of J1952 derived from the X-ray spectral fits (Table 2) with NS cooling models (Yakovlev & Pethick 2004), we find that the entire surface temperature of 80–90 eV provided by the atmospheric models is consistent with the standard cooling scenario for the obtained age range. For the BB model, a 3σ upper limit on the entire surface temperature of ≈ 60 eV appears to be cooler than the standard cooling scenario predicts, if J1952 age is $\lesssim 30$ kyr.

Arzoumanian et al. (2011) have noticed, that by many properties DA 495 is similar to the PWN G76.9+1.0 associated with the pulsar J2022+3842. Both objects demonstrate bright radio PWNe with similar morphologies, while their X-ray PWNe are faint, have much smaller sizes than in the radio and coincide with central faint emission holes of the radio PWNe. The ratio of the PWN sizes in the radio and X-rays is about 20 for both objects. As for DA 495, no SNR shell was found for G76.9+1.0. PSR J2022+3842 with $P = 48.6$ ms, detected in the radio and X-rays, has a characteristic age ≈ 8.9 kyr, $B \approx 2.1 \times 10^{12}$ G and $\dot{E} \approx 3 \times 10^{37}$ erg s $^{-1}$. Its PWN X-ray luminosity is $\approx 6 \times 10^{32}$ erg s $^{-1}$, assuming the distance of 10 kpc (Arzoumanian et al. 2011; Arumugasamy et al. 2014). Positions of PSR J2022+3842 and its PWN in Fig. 5, 6 are shown by triangles. Given the similarity between DA 495 and G76.9+1.0, one can suggest that DA 495 may also be as young as G76.9+1.0, which is consistent with the low boundary of the age range predicted by the $\dot{E} - L_{\text{pwn}}$ relation (see Fig. 6). For the simple synchrotron cooling model the minimum age is about 30 kyr at the minimum allowed distance of 1.3 kpc inferred from the X-ray fits. This demonstrates that the simple synchrotron cooling model does not work in this case. This is not a sur-

prise, as it cannot explain spectra of other PWNe also and is used only for rough estimates (e.g. Gaensler & Slane 2006).

Fermi/LAT recently detected at 6σ significance a γ -ray source 3FGL J1951.6+2926 coinciding spatially with DA 495 (Acero et al. 2015). Its spectrum is described by a power law with an exponential cut-off with an integral flux $\approx 10^{-11}$ erg cm $^{-2}$ s $^{-1}$ above 100 MeV. It was proposed as a possible DA 495 PWN γ -ray counterpart. However, comparing the source spectrum with the radio-X-ray spectrum of DA 495 compiled by us above, we find that such interpretation is hardly possible, since it would yield an unrealistically strong high energy excess in the PWN spectral energy distribution (SED) (Fig. 7) which is not predicted by any model of the PWN spectral evolution and not observed for most of evolved PWNe (e.g., Temim et al. 2013, 2015).

An exception is a composite SNR MSH 11-62 containing the PWN where similar excess is observed (Slane et al. 2012). To explain the excess with SNR models one needs to assume an unrealistically high ambient density for a hadronic scenario or an unreasonably large fraction of the SNR mechanical energy converted to relativistic particles for a leptonic scenario. The PWN model, in turn, requires an extremely high pulsar spin-down power. Based on that, Slane et al. (2012) suggested that such a strong γ -ray emission of the SNR likely arises from its pulsar.

Another unusual example is G76.9+1.0, the twin of DA 495 discussed above. Martin et al. (2014) modelled its spectrum and concluded that the detection of this PWN at the GeV–TeV range seems unexpected. Nevertheless, Acero et al. (2015) have reported on a possible γ -ray counterpart, 3FGL J2022.2+3840, of the G76.9+1.0 PWN. We find, that this implies similar unreasonably high energy excess in its SED as for DA 495 and MSH 11-62 (Fig. 8). At the same time, Pilia et al. (2011) have reported on a 5σ detection of the pulsed emission from PSR J2022+3842, associated with this PWN, at energies above 200 MeV with a pulsed flux of $(2.7 \pm 0.5) \times 10^{-7}$ photons cm $^{-2}$ s $^{-1}$. This flux is compatible with that reported by Acero et al. (2015) for

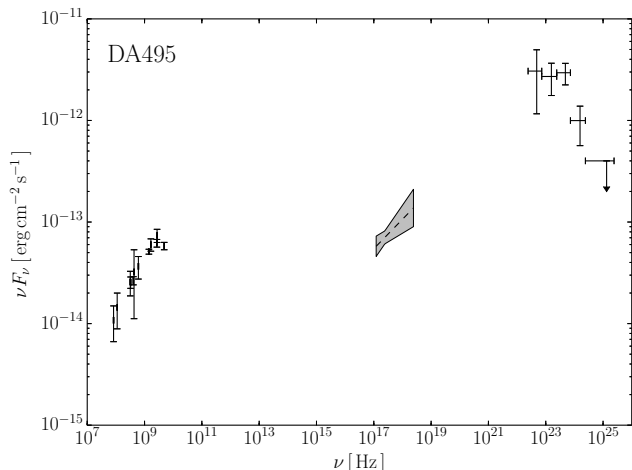


Figure 7. Radio and X-ray SED of the DA 495 PWN and the GeV spectrum of the associated *Fermi* source 3FGL J1951.6+2926.

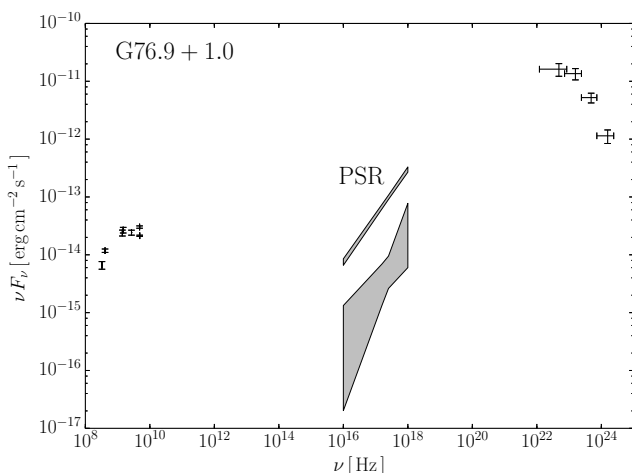


Figure 8. Radio and X-ray SED of the G76.9+1.0 PWN and the GeV spectrum of 3FGL J2022.2+3840, presumably the associated pulsar J2022+3842. The X-ray spectrum of the pulsar, marked by PSR, is shown for comparison. The γ -ray emission level in respect to the radio-X-ray SED is similar to that of DA 495.

3FGL J2022.2+3840, suggesting that both groups observed the same object. For the distance of 10 kpc, this yields the pulsar luminosity $L_\gamma = (3.6 \pm 0.6) \times 10^{35}$ erg s $^{-1}$ and the γ -efficiency $L_\gamma/\dot{E} \approx 0.01$. 3FGL J2022.2+3840 has also the power law spectrum with the exponential cut-off typical for other *Fermi* pulsars (Abdo et al. 2013).

The DA 495 SED similarity with those of G76.9+1.0 and MSH 11-62 implies that the associated *Fermi* source 3FGL J1951.6+2926 is likely the γ -ray counterpart of the J1952 pulsar but not of the PWN. This is also supported by the pulsar-like spectrum of the source. In this case, the pulsar luminosity $L_\gamma \approx 10^{34}$ erg s $^{-1}$ for the distance of 3 kpc. Given that, and assuming the same γ -efficiency as for PSR J2022+3842, we obtain $\dot{E} \approx 10^{36}$ erg s $^{-1}$ for J1952, which is within the range obtained above using the X-ray data.

7 SUMMARY

The X-ray spectrum of J1952 is pure thermal and can be described either by the BB or NS atmosphere models. In the former case the emission comes from a pulsar hot spot and in the latter – from a bulk of the NS surface with $T \approx 85$ eV consistent with standard NS cooling scenarios. The $N_{\text{H}}-D$ relation provides independent constraints on the distance to the object. For atmosphere models it can be larger, up to 5 kpc, than it was supposed early. The upper limit for the pulsed emission fraction of J1952 is 40 per cent at 99 per cent confidence. It does not help to discriminate whether the thermal emission originates from the hot spot or the bulk of the NS surface. The derived PWN X-ray luminosity range and the pulsar nonthermal luminosity upper limit combined with those of other pulsar+PWN systems imply the DA 495 age of 7–155 kyr. Empirical relations between \dot{E} , L_{pwn} , $L_{\text{psr}}^{\text{pl}}$ and age predict a possible J1952 $\log \dot{E}$ range of 34.7–37.1. The BB model for J1952 suggests that the PWN spectrum likely becomes flatter in X-rays than in the radio above a break near 2 GHz, suggesting a second high frequency spectral break. The atmosphere models do not require the second break. Sub-millimetre and infrared observations could help to check that. We suggest, that 3FGL J1951.6+2926 is the likely γ -ray counterpart of the J1952 pulsar. To constrain J1952 energetics and age, deeper X- and γ -ray timing observations are needed.

ACKNOWLEDGMENTS

The scientific results reported in this article are based on data obtained from the *Chandra* Data Archive and observations obtained with *XMM-Newton*, an ESA science mission with instruments and contributions directly funded by ESA Member States and the USA (NASA). We thank the anonymous referee for useful comments and Dmitrii Barsukov and Denis Baiko for helpful discussion. The work of AK and DZ was supported by RF Presidential Programme MK-2837.2014.2. YS acknowledges the support from Russian Foundation for Basic Researches (grant 14-02-00868-a).

Facilities: CXO, XMM.

REFERENCES

- Abdo A. A., et al., 2013, *ApJS*, **208**, 17
- Acero F., et al., 2015, *ApJS*, **218**, 23
- Anders E., Grevesse N., 1989, *Geochim. Cosmochim. Acta*, **53**, 197
- Arumugasamy P., Pavlov G. G., Kargaltsev O., 2014, *ApJ*, **790**, 103
- Arzoumanian Z., Safi-Harb S., Landecker T. L., Kothes R., 2004, *ApJ*, **610**, L101
- Arzoumanian Z., Safi-Harb S., Landecker T. L., Kothes R., Camilo F., 2008, *ApJ*, **687**, 505
- Arzoumanian Z., Gotthelf E. V., Ransom S. M., Safi-Harb S., Kothes R., Landecker T. L., 2011, *ApJ*, **739**, 39
- Balucinska-Church M., McCammon D., 1992, *ApJ*, **400**, 699
- Bietenholz M. F., Bartel N., 2008, *MNRAS*, **386**, 1411
- Chevalier R. A., Reynolds S. P., 2011, *ApJ*, **740**, L26
- Foreman-Mackey D., Hogg D. W., Lang D., Goodman J., 2013, *PASP*, **125**, 306
- Gaensler B. M., Slane P. O., 2006, *ARA&A*, **44**, 17

- Galt J. A., Kennedy J. E. D., 1968, *AJ*, **73**, 135
- Gelfand J. D., Slane P. O., Zhang W., 2009, *ApJ*, **703**, 2051
- Ginzburg V. L., Syrovatskii S. I., 1965, *ARA&A*, **3**, 297
- Gonzalez M., Safi-Harb S., 2003, *ApJ*, **591**, L143
- Goodman J., Weare J., 2010, *Comm. App. Math. Comp. Sci.*, **5**, 65
- Ho W. C. G., Potekhin A. Y., Chabrier G., 2008, *ApJS*, **178**, 102
- Kargaltsev O., Pavlov G. G., 2008, in Bassa C., Wang Z., Cumming A., Kaspi V. M., eds, American Institute of Physics Conference Series Vol. 983, 40 Years of Pulsars: Millisecond Pulsars, Magnetars and More. pp 171–185 ([arXiv:0801.2602](#)), [doi:10.1063/1.2900138](#)
- Kennel C. F., Coroniti F. V., 1984, *ApJ*, **283**, 710
- Kirichenko A., et al., 2015, *ApJ*, **802**, 17
- Kothes R., Landecker T. L., Wolleben M., 2004, *ApJ*, **607**, 855
- Kothes R., Landecker T. L., Reich W., Safi-Harb S., Arzoumanian Z., 2008, *ApJ*, **687**, 516
- Landecker T. L., Caswell J. L., 1983, *AJ*, **88**, 1810
- Li X.-H., Lu F.-J., Li Z., 2008, *ApJ*, **682**, 1166
- Marshall D. J., Robin A. C., Reylé C., Schultheis M., Picaud S., 2006, *A&A*, **453**, 635
- Martin J., Torres D. F., Cillis A., de Oña Wilhelmi E., 2014, *MNRAS*, **443**, 138
- Migliazzo J. M., Gaensler B. M., Backer D. C., Stappers B. W., van der Swaluw E., Strom R. G., 2002, *ApJ*, **567**, L141
- Ng C.-Y., Romani R. W., Brisken W. F., Chatterjee S., Kramer M., 2007, *ApJ*, **654**, 487
- Pavlov G. G., Zavlin V. E., 2000, in Martens P. C. H., Tsuruta S., Weber M. A., eds, IAU Symposium Vol. 195, Highly Energetic Physical Processes and Mechanisms for Emission from Astrophysical Plasmas. p. 103
- Pilia M., Treves A., Pellizzoni A., Trois A., Motta S., 2011, The Astronomer's Telegram, **3466**, 1
- Predehl P., Schmitt J. H. M. M., 1995, *A&A*, **293**, 889
- Reid M. J., et al., 2014, *ApJ*, **783**, 130
- Rieke G. H., Lebofsky M. J., 1985, *ApJ*, **288**, 618
- Roberts M. S. E., Tam C. R., Kaspi V. M., Lyutikov M., Vasisht G., Pivovarov M., Gotthelf E. V., Kawai N., 2003, *ApJ*, **588**, 992
- Robin A. C., Reylé C., Derrière S., Picaud S., 2003, *A&A*, **409**, 523
- Slane P., et al., 2012, *ApJ*, **749**, 131
- Tanaka S. J., Takahara F., 2010, *ApJ*, **715**, 1248
- Temim T., Slane P., Castro D., Plucinsky P. P., Gelfand J., Dickel J. R., 2013, *ApJ*, **768**, 61
- Temim T., Slane P., Kolb C., Blondin J., Hughes J. P., Bucciantini N., 2015, preprint, ([arXiv:1506.03069](#))
- Vaughan B. A., et al., 1994, *ApJ*, **435**, 362
- Xu Y., et al., 2013, *ApJ*, **769**, 15
- Yakovlev D. G., Pethick C. J., 2004, *ARA&A*, **42**, 169
- Zavlin V. E., 2007, Thermal emission from isolated neutron stars: theoretical and observational aspects ([arXiv:astro-ph/0702426](#))
- Zavlin V. E., Pavlov G. G., Shibano Y. A., 1996, *A&A*, **315**, 141